15 November 2001

ELSEVIER

Optics Communications 199 (2001) 143–148

OPTICS COMMUNICATIONS

www.elsevier.com/locate/optcom

A generalization of Abel inversion to non-axisymmetric density distribution

P. Tomassini *, A. Giulietti

Istituto di Fisica Atomica e Molecolare, CNR Area della Ricerca di Pisa, Via G. Moruzzi, 56124 Pisa, Italy

Received 21 May 2001; accepted 6 September 2001

Abstract

Abel inversion is currently used in laser-plasma studies in order to estimate the electronic density n_e from the phase-shift map $\delta\phi$ obtained via interferometry. The main limitation of the Abel method is due to the assumption of axial symmetry of the electronic density, which is often hardly fulfilled. In this paper we present an improvement to the Abel inversion technique in which the axial symmetry condition is relaxed by means of a truncated Legendre polynomial expansion in the azimuthal angle. With the help of simulated interferograms, we will show that the generalized Abel inversion generates accurate densities maps when applied to non-axisymmetric density sources. © 2001 Published by Elsevier Science B.V.

PACS: 52.70.−m

Keywords: Plasma diagnostics; Interferometry

Abel inversion is widely used in many context and, in laser-plasma studies it leads to a 2D electronic density map n_e reconstruction from phase-shift maps $\delta\phi$ recorded using interferometry [1,2]. Once the phase map $\delta\phi(z,x)$ has been extracted from the interferogram via standard FFT techniques [3] or with a more sophisticated wavelet-based method [4], the best symmetry axis z_0 should be defined and two half-space phase maps

$$\begin{aligned}\delta\phi^+(\zeta,x) &= \delta\phi(z-z_0,x) \quad z > z_0,\\ \delta\phi^-(\zeta,x) &= \delta\phi(z_0-z,x) \quad z < z_0\end{aligned} \tag{1}$$

are introduced. By assuming axial symmetry around the laser-beam propagation axis x, $\delta\phi^+ = \delta\phi^-$ so the electronic density map $n_e(r,x)$ is computed as

$$n_e(r,x) = -n_c \frac{\lambda_p}{\pi^2} \int_r^\infty d\zeta \frac{1}{\sqrt{\zeta^2 - r^2}} \frac{\partial}{\partial\zeta} \delta\phi^{\pm}(\zeta,x), \tag{2}$$

where λ_p is the probe wavelength and $n_c = \pi m(c/e\lambda_p)^2$ is the critical density at λ_p.

Though laser plasmas show approximately axial symmetry in general, significant deviations from the symmetry may occur. In these latter cases the Abel inversion applied to an artificial profile obtained by symmetrization of either $\delta\phi^+$ or $\delta\phi^-$, can lead to misleading reconstruction of the density distribution. Alternately, to consider the "mean"

* Corresponding author. Tel.: +39-050-315-2256; fax: +39-050-315-2230.

E-mail address: tomassini@ifam.pi.cnr.it (P. Tomassini).

0030-4018/01/$ - see front matter © 2001 Published by Elsevier Science B.V.
PII: S0030-4018(01)01575-9

phase distribution $\delta\phi_s = 1/2(\delta\phi^+ + \delta\phi^-)$ can also induce large errors.

In 1981 Yasutomo [5] presented a generalization of Abel inversion based on the assumption that the 3D density distribution $n(r,x,\theta)$ can be factorized as the product of a isotropic density $\tilde{n}_0(r)$ and a corrective term $g(r\sin\theta)$, being θ the azimuthal angle.

In this paper we introduce a generalization of the Abel inversion algorithm to be applied to moderately asymmetric interferograms. Unlike Yasutomo, we base our algorithm on a Legendre polynomial expansion of $n(r,x,\theta)$ in the angular variable alone. We will show that such an extension of the Abel method allows accurate reconstructions of the density distribution in some simulated non-symmetric cases.

The basic geometry of the phase-shift acquisition via interferometry is shown in Fig. 1, in which a plane parallel to the laser propagation axis (x-direction) (Fig. 1(a)), and a plane perpendicular to that axis (Fig. 1(b)), are shown, respectively.

Let us point out that any departure from the mirror symmetry respect to the plane perpendicular to the probe axis (the x–z plane in Fig. 1) cannot be taken into account because of the line integral in the acquisition step. Consequently we can assume that such a mirror symmetry is satisfied.

The phase-shift $\delta\phi(z,x)$ detected in the (z,x) position on the interferogram is then linked to the electronic density $n_e(r,\theta,x)$ as

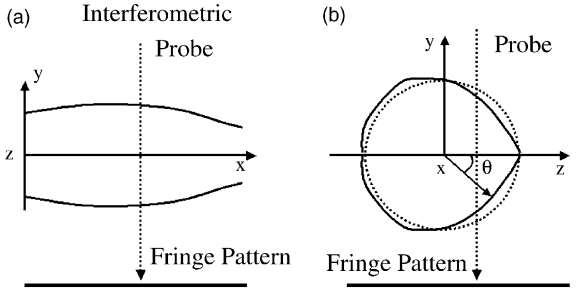

Fig. 1. (a) Formation of an interferogram. The symmetry axis is x and the phase shift is obtained integrating over the y-direction. (b) Because of an integration along the y-axis, no departure of n_e from a mirror-symmetric distribution can be detected.

$$\begin{aligned}\delta\phi(z,x) &= -\frac{\pi}{\lambda_p}\int_{-\infty}^{\infty}\frac{n(z,y,x)}{n_c}\,dy \\ &= -\frac{2\pi}{\lambda_p}\int_{|z-z_0|}^{\infty}\frac{r}{\sqrt{r^2-(z-z_0)^2}} \\ &\quad\times\frac{n(r,\theta(r),x)}{n_c}\,dr,\end{aligned} \tag{3}$$

where we moved to the cylindrical coordinates (r,θ), taking x as symmetry axis.

We now make the physically justified assumption that the angular dependence of $n_e(r,\theta,x)$ is everywhere "well behaved" (no abrupt changes occur) so that n_e can be developed as a truncated series of orthonormal Legendre polynomials $P_l(\cos(\theta))$:

$$n_e(r,\theta,x) = \sum_{l=0}^{L} n_l(r,x)P_l(\cos(\theta)). \tag{4}$$

To find the appropriate value of L, let us simply observe that for each x from $\delta\phi^+(\zeta)$ and $\delta\phi^-(\zeta)$ we can build up two linearly independent sequences

$$\delta\phi_s \equiv \tfrac{1}{2}\big(\delta\phi^+(\zeta) + \delta\phi^-(\zeta)\big),$$

$$\delta\phi_a \equiv \tfrac{1}{2}\big(\delta\phi^+(\zeta) - \delta\phi^-(\zeta)\big)$$

so that for each x and r we have *two* independent degrees of freedom which could be linked to the angular dependence and this leads to $L = 1$. The truncation of the series of Eq. (4) up to $l = 1$ is straightforward. Since $P_0(x) = 1$ and $P_1(x) = x$, we have

$$n(r,\theta,x) = n_0(r,x) + n_1(r,x)\cos(\theta) \tag{5}$$

and so the phase-shift map is computed as

$$\begin{aligned}\delta\phi(z,x) &= -\frac{2\pi}{\lambda_p}\int_{|z-z_0|}^{\infty}\frac{r}{\sqrt{r^2-(z-z_0)^2}}\frac{1}{n_c} \\ &\quad\times\left\{n_0(r,x) + n_1(r,x)\frac{(z-z_0)}{r}\right\}dr.\end{aligned} \tag{6}$$

Defining $v_1(r,x) \equiv n_1(r,x)/r$ and extracting the symmetric and antisymmetric components of $\delta\phi$ in Eq. (6), we obtain

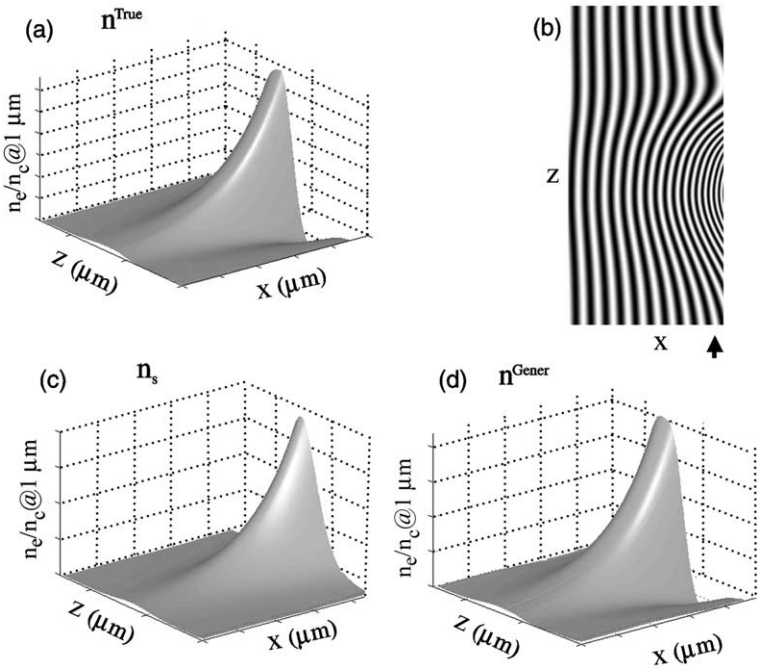

Fig. 2. (a) The z–x plane projection of the simulated electronic density. The radial profile is of the form $n^{\mathrm{True}} = n_0P_0 + n_1P_1 + n_2P_2$, while the density is exponentially decreasing in the longitudinal direction. (b) The simulated interferogram obtained with the density map n^{True} and $\lambda_{\mathrm{p}} = 1$ μm. (c, d) Projections onto the z–x plane of the density maps obtained with the standard and generalized Abel inversion of the phase shift of the simulated interferogram (b).

$$\begin{aligned}\delta\phi_{\mathrm{s}}(\zeta,x) &= -\frac{\pi}{\lambda_{\mathrm{p}}}\int_{\zeta}^{\infty}\frac{r}{\sqrt{r^2-\zeta^2}}\frac{n_0(r,x)}{n_{\mathrm{c}}}\mathrm{d}r,\\ \delta\phi_{\mathrm{a}}(\zeta,x) &= -\frac{\pi\zeta}{\lambda_{\mathrm{p}}}\int_{\zeta}^{\infty}\frac{r}{\sqrt{r^2-\zeta^2}}\frac{v_1(r,x)}{n_{\mathrm{c}}}\mathrm{d}r\end{aligned} \tag{7}$$

and we can finally invert Eq. (7) obtaining the coefficients of the generalized Abel inversion:

$$\begin{aligned}n_0(r,x) &= -n_{\mathrm{c}}\frac{\lambda_{\mathrm{p}}}{\pi^2}\int_{r}^{\infty}\mathrm{d}\zeta\frac{1}{\sqrt{\zeta^2-r^2}}\frac{\partial}{\partial\zeta}\delta\phi_{\mathrm{s}}(\zeta,x),\\ n_1(r,x) &= -n_{\mathrm{c}}\frac{\lambda_{\mathrm{p}}}{\pi^2}r\int_{r}^{\infty}\mathrm{d}\zeta\frac{1}{\sqrt{\zeta^2-r^2}}\frac{\partial}{\partial\zeta}\left(\frac{\delta\phi_{\mathrm{a}}(\zeta,x)}{\zeta}\right).\end{aligned} \tag{8}$$

The application of the generalized Abel inversion (Eqs. (5) and (8)) is straightforward and very effective. In order to prove this, the new algorithm will be tested with two sample interferograms. Both of them have been obtained numerically from a priori known density distributions, with which the reconstructed distributions can be compared.

Let us firstly consider the sample interferogram of Fig. 2(b), obtained from the 3D density distribution of the form $n^{\mathrm{True}}(r,\theta,x) = n_0(r,x)\times P_0(\cos(\theta)) + n_1(r,x)P_1(\cos(\theta)) + n_2(r,x)P_2(\cos(\theta))$, with n_i Gaussian shaped in the radial direction r and exponentially decreasing in the longitudinal direction x. The simulation is performed assuming a 1 μm wavelength probe and a maximum density of n_i in n_{c} units as $n_0^{\max} = 0.1$, $n_1^{\max} = 0.05$, $n_2^{\max} = 0.025$.

Once the phase-shift $\delta\phi$ has been extracted from the interferogram, an automatic procedure to optimize the position of the global symmetry axis (z_0) has been applied and the two half phase maps $\delta\phi^+$ and $\delta\phi^-$ have been constructed. Next, the electronic densities $n^+(r,x)$, $n^-(r,x)$, $n^{\mathrm{mean}}(r,x)$ are computed via standard Abel inversion applied to $\delta\phi^+$, $\delta\phi^-$, $\delta\phi_{\mathrm{s}} = 1/2(\delta\phi^+ + \delta\phi^-)$, respectively. Finally, the generalized Abel inversion (Eqs. (5)

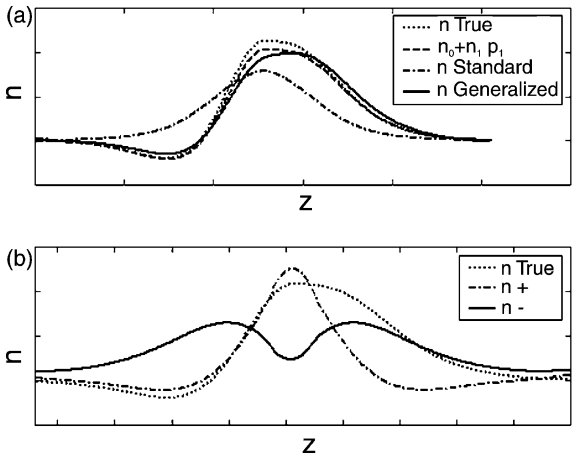

Fig. 3. (a) Line outs of the z–x projection of the true density profile (dotted line), the sum of the P_0 and P_1 terms (dashed line) and of density profiles obtained via standard Abel inversion of $\delta\phi_s$ (the mean of $\delta\phi^+$ and $\delta\phi^-$) and of the generalized Abel inversion. The generalized Abel inversion is considerably more accurate than standard inversion. (b) Line outs of the z–x projection of the density profiles obtained via standard Abel inversion of $\delta\phi^+$ and $\delta\phi^-$. None of them well reproduces the true density profile (dotted line).

and (8)) is applied to both $\delta\phi^+$ and $\delta\phi^-$ producing $n^{\mathrm{Gener}}(r,\theta,x)$.

In Fig. 2 projections onto the z–x plane of the simulated density (a), the standard Abel inversion of the symmetrized map $\delta\phi_s$ (c) and of the generalized Abel inversion of $\delta\phi^+$ and $\delta\phi^-$ (d), are shown. As it is clear, n^{mean} shape differs considerably from the one of n^{True}, while n^{Gener} well match the true density map. For a more quantitative comparison, we have reproduced in Fig. 3(b) line outs of the projection of the true density map n^{True} and of n^+ and n^- at $x = 10$ μm from the simulated target. As it is evident, not only none of them reasonably reproduces the true density contour but their shapes also differ very much. As a result, standard Abel inversion is not applicable in this case in order to produce a (reasonably) accurate density map. In Fig. 3(a) the line outs of the projection of the generalized Abel inversion n^{Gener} and the standard inversion of $\delta\phi_s$ are confronted with the true density contour (dotted line) and $n_{01} \equiv n_0P_0 + n_1P_1$ (dashed line). Standard Abel inversion applied to the mean phase-shift map still fails in reproducing a reasonable density map, while generalized Abel inversion gives us a contour which is everywhere well overlapped to the true one. Now, as a result, we can claim that with the use of the generalized Abel inversion a good estimation of the simulated density map is achieved.

Now, let us test the new algorithm in a physical condition which is often experimentally observed: a density with an axially symmetric background to which it is added an axially symmetric channel whose symmetry axis is not aligned with the one of the background (see Fig. 4(a)). As before, the maximum electronic density is well below the critical density $n_{\mathrm{max}}^{\mathrm{True}} = 0.1n_c$ and the probe wavelength is 1 μm.

As in the previous example we apply the standard and the generalized Abel inversions to the phase-shift maps extracted by the interferogram reproduced in Fig. 4(b). In Fig. 4(c) and (d), the best output of the standard Abel inversion (the one obtained with $\delta\phi_+$) and of the generalized Abel inversion are shown, respectively. As in the previous example, standard Abel inversion produces a poorly accurate density map. A more quantitative analysis can be performed with the help of line outs reported in Fig. 5, which shows that standard Abel inversion results should be rejected. On the contrary, generalized Abel inversion produces reasonably good results in almost all the density map but a thin band near the best symmetry axis, where the dependence of n^{True} on $\cos(\theta)$ is much more complex than linear.

We face now with a noisy phase map in order to compare the noise content in the standard and in the generalized Abel inversions. Here we will focus only on Gaussian and uncorrelated (white) noise, which is added to the phase-shift map of the interferogram reproduced in Fig. 4(b) (see Fig. 6(a)). To visualize the noise which is propagated to the density maps n_0^{Noise} and n_1^{Noise} (see Fig. 4(b)), we subtract them to the density maps n_0 and n_1 we have previously computed with the phase map of interferogram in Fig. 4(b) (in which no noise were introduced). The resulting error maps $\delta n_0 = n_0 - n_0^{\mathrm{Noise}}$ and $\delta n_1 = n_1 - n_1^{\mathrm{Noise}}$ are finally confronted. Since the isotropic component of the density map n_0^{Noise} coincides with the standard Abel inversion of the symmetrized phase map, we can compare the noise content in the standard and in the generalized

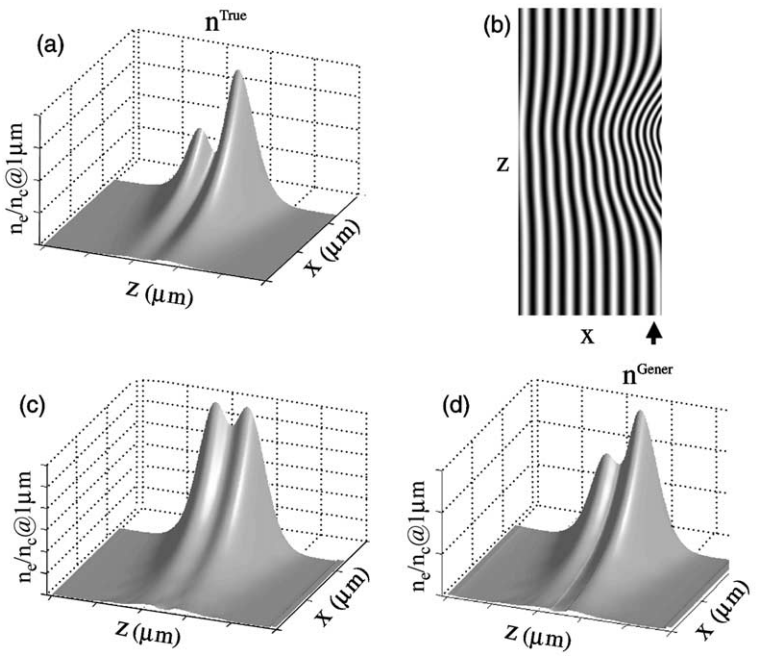

Fig. 4. (a) The z–x plane projection of the simulated electronic density. The radial profile is the sum of a background and a channel not aligned with its symmetry axis, while the density is exponentially decreasing in the longitudinal direction. (b) The simulated interferogram obtained with the density map n^{True} and $\lambda_p = 1$ μm. (c) Projection onto the z–x plane of the density maps obtained with the standard Abel inversion of $\delta\phi^+$ and (d) projection of generalized Abel inversion.

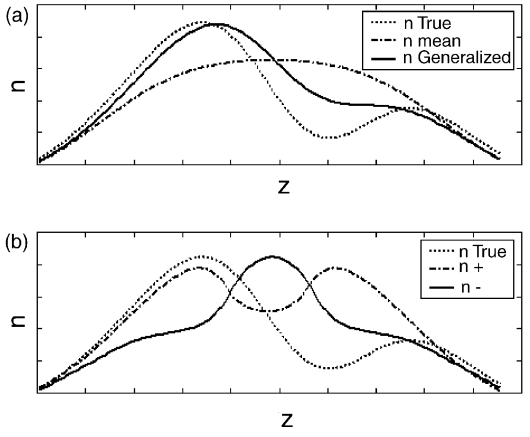

Fig. 5. (a) Line outs of the z–x projection of the true density profile (dotted line) and of density profiles obtained via standard Abel inversion of $\delta\phi_s$ (dashed line) and of the generalized Abel inversion (continuous line). The generalized Abel inversion is considerably more accurate than standard inversion. (b) Line outs of the z–x projection of the density profiles obtained via standard Abel inversion of $\delta\phi^+$ (dashed line) and $\delta\phi^-$ (continuous line). None of them well reproduces the true density profile (dotted line).

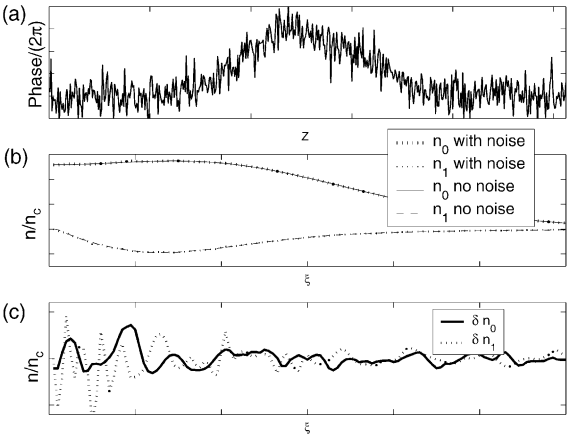

Fig. 6. (a) Line out of the noisy phase-shift map, obtained by summing up the phase-shift map of the interferogram in Fig. 4 and a Gaussian white noise map. (b) Line outs of the resulting density maps n_0^{Noise} and n_1^{Noise} obtained via generalized Abel inversion. Line outs of the n_0 and n_1 maps generated by inverting the noise free map are reported as a reference. (c) Line outs of δn_0 and δn_1. The *rms* of the two noise sequences is comparable so the noise content of n_0^{Noise} and n_1^{Noise} is similar.

inversions by simply comparing the noise in n_0^{Noise} and n_1^{Noise}. In Fig. 6(c) line outs of δn_0 and δn_1 are reproduced.

Since the density maps are obtained integrating the uncorrelated noise with a kernel $1/(\zeta^2 - r^2)^{1/2}$ which is rising in approaching the symmetry axis ($r \to 0$), we expect a noise sequence with a stronger component near $r = 0$. Furthermore, in computing n_1 (see Eq. (8)) we face with the derivative of $(\delta\phi_a(\zeta, x)/\zeta)$, so that the $1/\zeta$ term will contribute to enhance the noise in the $r \to 0$ region. Nevertheless, because of the regularization induced by the overall multiplication by r, a balancing of the two effects occur and the noise observed onto the n_1^{Noise} map is comparable with the one of the standard Abel inversion n_0^{Noise} map, as it is clear in Fig. 6(c).

To conclude, the generalized Abel inversion method we propose is very simple and effective, *it uses consistently the information carried by the whole phase-shift map* and, as shown in the examples, it can be successfully applied to asymmetric cases for which the standard method based on only half-space phase-shift map, fails.

Acknowledgements

One of the authors (P.T.) wish to acknowledge support from the Italian MURST (Project: "Metodologie e diagnostiche per materiali e ambiente"). Authors are very grateful to D. Giulietti, from the Department of Physics, University of Pisa and to L.A. Gizzi and R. Numico from IFAM-CNR, Pisa, for useful discussions and their encouragement.

References

[1] M.G. Nomarski, Journal de la Physique et le Radium 16 (1955) 95.
[2] L.A. Gizzi et al., Phys. Rev. E 49 (1994) 5628 (Erratum: Phys. Rev. E 50 (1994) 4266).
[3] K.A. Nugent, Appl. Opt. 18 (1985) 3101.
[4] P. Tomassini et al., Analyzing laser-plasma interferograms with a continuous wavelet transform ridge extraction technique: the method, Appl. Opt., in press (preprint on xray.ifam.pi.cnr.it).
[5] Y. Yasutomo, IEEE Trans. Plasma Sci. PS-9 (1981) 18–21.